Physics of vacuum generation in zero-secondary flow ejectors

R. Arun Kumar, and G. Rajesh

Articles you may be interested in

Bubble dynamics and atomization mechanisms in burning multi-component droplets
Physics of Fluids **30**, 067101 (2018); 10.1063/1.5035384

Towards enhanced bubble detachment within a thin liquid film by electrowetting with voltage modulation
Physics of Fluids **30**, 062102 (2018); 10.1063/1.5031430

Effect of gap flow on the shallow wake of a sharp-edged bluff body—Coherent structures
Physics of Fluids **30**, 065107 (2018); 10.1063/1.5022252

Influence of vorticity distribution on singularities in linearized supersonic flow
Physics of Fluids **30**, 056105 (2018); 10.1063/1.5030091

Compressible liquid flow in nano- or micro-sized circular tubes considering wall–liquid Lifshitz–van der Waals interaction
Physics of Fluids **30**, 062002 (2018); 10.1063/1.5023291

Pattern selection in miscible liquids under periodic excitation in microgravity: Effect of interface width
Physics of Fluids **30**, 062103 (2018); 10.1063/1.5032107

Physics of vacuum generation in zero-secondary flow ejectors

R. Arun Kumar and G. Rajesh[a)]
Department of Aerospace Engineering, Indian Institute of Technology Madras, Chennai 600036, India

This paper aims to investigate the secondary flow characteristics and the associated vacuum generation caused with increase in the primary pressure ramping in zero-secondary flow ejectors. The sudden expansion of the primary jet into the diffuser during the ejector start-up results in flow separation from the shear layer formed between the primary and inducted flows and produces large recirculation bubbles in the top and bottom sides of the jet. These recirculation bubbles cause an induced flow from ambient air into the diffuser duct as well. The fluid supply from the reverse flow due to the shear layer separation and the induced flow from ambient air provide a counter momentum against fluid entrainment from a vacuum chamber. As a result of this, the initial vacuum generation process progresses in a slow rate. Thereafter, the primary jet expansion reaches a critical level and a rapid vacuum generation can be seen. It is found that with the jet expansion reaching a critical level, the fluid supply from the reverse flow is suddenly entrained back into the main jet at the maximum jet expansion point. This suddenly reduces the counter-momentum which has been prohibiting the entrainment of fluid from the vacuum chamber and results in rapid evacuation. This is followed by a stage in which the vacuum chamber pressure is increasing due to the attainment of a constant Mach number at the diffuser inlet and the jet pressure ramping. It is found that the secondary flow dynamics and the vacuum generation processes in rectangular and round ejectors show a close resemblance. *Published by AIP Publishing.* https://doi.org/10.1063/1.5030073

I. INTRODUCTION

It is well known that a high momentum jet exhibits self-pumping characteristics, whereby it entrains the surrounding secondary stream due to the momentum exchange and shearing action between the two streams. This principle is being widely used for various industrial applications such as fluid mixing,[1,2] fluid transportation,[3] thrust augmentation,[4,5] refrigeration systems,[6,7] and noise reduction,[8] and such devices which employ this principle are generally termed as ejectors. The geometry of an ejector thus requires a primary duct to supply the high momentum fluid, a secondary duct through which secondary stream induction happens, a mixing section where the two fluids mix, and a subsonic diffuser through which pressure recovery occurs. In supersonic ejectors, the mixing section, which is usually a straight duct, also functions as a diffuser since the shock wave structures in the mixed supersonic flow help in pressure recovery. Another prominent application of the ejector systems is vacuum generation.[9,10] This is done by entraining/inducting fluid from a closed secondary chamber by utilizing the self-pumping action of the primary jet, as shown in Fig. 1. The ejectors used for generating vacuum conditions are called vacuum ejectors or zero secondary flow ejectors.

Vacuum ejectors are commonly used in high altitude testing (HAT) facilities to create controlled vacuum back pressures to simulate upper atmospheric conditions in rocket motors.[11] Very large pressure ratios required in hypersonic test facilities are produced by reducing the nozzle exit pressure conditions

using the vacuum ejector principle.[12] In both the above facilities, the primary nozzle jet momentum itself can be used to create the required low back pressure conditions. Depending on the application, vacuum ejectors operate in two modes. In HAT and hypersonic test facilities, it is desired to expand the primary jet completely to the diffuser wall and this mode of operation is known as the started mode.[13] In vacuum pumps, it is desired that the primary jet does not completely expand to the diffuser wall and this mode of operation is termed as the un-started mode.[13]

In the past, significant amount of studies have been carried out to optimize the performance of vacuum ejectors, particularly to optimize the starting mode pressure (primary jet total pressure required to achieve the started mode, P_{0s}) and to enhance the minimum secondary vacuum pressure levels (P_s).[13–18] German and Bauer[13] investigated the effect of diffuser length on the vacuum ejector performance, and they found that there exists an optimum diffuser length for which the starting mode pressure is minimum, and after this length, the started mode pressure remains constant. Annamalai *et al.*[16] carried out a parametric study on the performance of the vacuum ejector by varying the geometric features such as the ratio of straight diffuser length to its diameter (L/D) and ratio of straight diffuser area to nozzle throat area (A_d/A_t). They observed that the starting mode pressure decreases with increase in the diffuser length and decrease in the diffuser height. Kumaran *et al.*[17] performed an optimization study and performance evaluation on vacuum ejectors with a second throat exhaust diffuser (STED). Ashok *et al.*[18] also proposed some effective ways to arrest the backflow into the secondary chamber, and they found

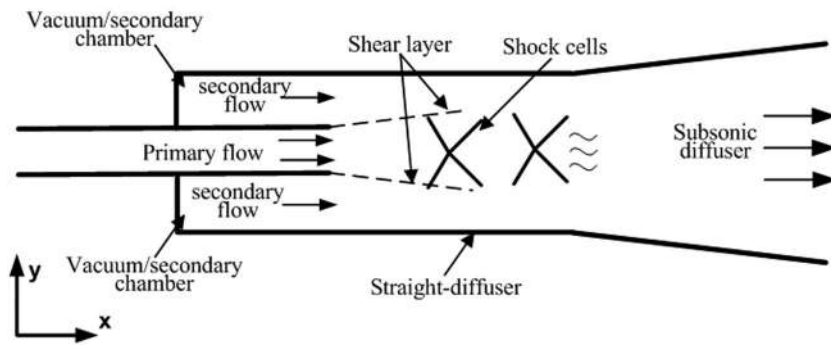a)Electronic mail: rajesh@ae.iitm.ac.in

FIG. 1. Schematic of the zero secondary flow/vacuum ejector-diffuser system.

that the back flow arresters help in a much faster ejector starting.

It is to be noted that all these optimization studies have been carried out after the primary jet total pressure becomes steady. However, in vacuum ejector-diffuser systems, there exists a transient start-up phase where the primary jet total pressure is being ramped from the atmospheric condition to the required operating condition (primary valve opening process). It is important to understand the fluid dynamics during this transient start-up period since the flow transients during this period might decide the level of vacuum and the performance of other sub-components involved in the system. However, it is seen from the past literature that there have been very few studies on the transient flow dynamics during vacuum ejector start-up, while performance optimization studies are in plenty.

In vacuum ejectors, the secondary and primary jet flow characteristics are highly coupled to each other during the transient start-up phase since the back pressure to which the primary jet expands continuously reduces with the progress in the secondary fluid entrainment process and vice versa. As a result of this, the physics of the vacuum ejector flow will be much more complicated compared to that of conventional steady ejectors. Previous studies with experimental pressure measurements reported that the vacuum chamber pressure exhibits large scale oscillations during the initial start-up period.[16,19] These secondary flow fluctuations are predominant when the primary jet expansion is such that it does not expand to the diffuser wall (un-started mode). Arun Kumar and Rajesh[19] proposed that the secondary oscillations during the un-started mode are associated with the recirculation bubbles existing in the diffuser. A computational study by Park et al.[20] also reported the presence of a recirculation bubble in the diffuser section. A numerical study by Mittal et al.[21] also confirmed the presence of the recirculation bubble in the diffuser. They also reported that the recirculation bubble extends and retracts from the secondary chamber during the initial vacuum ejector start-up period, causing the secondary flow to move to and fro into the secondary chamber. After the transient start-up period of the vacuum ejector, a steady state operation is achieved in which there is no secondary induction, but the shear layer still persists. Lijo et al.[22] proposed that for steady state vacuum ejectors operated at the un-started mode, the shear layer is maintained by the large recirculation bubbles which exist in the secondary stream.

From all the above studies on the fluid dynamic aspect of vacuum ejectors, it can be confirmed that recirculation bubbles are formed in the secondary stream inducted from the vacuum chamber during the un-started mode and the nature of recirculation plays a major role in vacuum chamber pressure oscillations and vacuum build-up. The recirculation bubbles in the diffuser can communicate to the vacuum chamber and thereby influence the vacuum levels only when the ejector operates in the un-started mode since the vacuum chamber is open to the diffuser downstream. Previous studies thus reported that the vacuum chamber pressure oscillations vanish only when the diffuser reaches started mode operation.[16,17] At started mode, the impingement of the primary jet with the diffuser wall creates oblique shock waves, and this impingement seals the vacuum chamber from any diffuser downstream perturbations. However, a recent experimental study by Arun Kumar and Rajesh[19] revealed that the secondary fluctuations cease before the onset of the started mode, which is in contrary to the previous understanding. The ceasing of secondary fluctuations is then followed by a rapid secondary evacuation. This rapid secondary evacuation stops when the ejector attains the started mode. They proposed that the ceasing of secondary fluctuations and the onset of rapid secondary evacuation are caused by the secondary flow choking in the diffuser when the primary jet expansion reaches a critical level.

From all these previous studies pertaining to the fluid dynamics in secondary chamber vacuum generation, it is seen that the secondary chamber pressure decreases non-monotonically with increasing primary pressure and there exist very large pressure perturbations during the initial start-up. Many of them unanimously suggest that the large-scale secondary perturbations during the initial start-up are associated with the recirculation bubbles existing in the diffuser, and also the recirculation bubbles play a deterministic role in the amount of "clean" vacuum (without any pressure oscillations) generated. However, these studies which claim this were mainly numerically oriented and provided only a steady state flow scenario in which the transient evolution of the recirculation bubbles is hardly investigated. The presence of the recirculation bubbles must hence be verified experimentally, and its influence on the transient development of vacuum, especially the rapid vacuum generation, in the chamber needs to be investigated in a comprehensive manner. Hence, in this study, we attempt to understand the fundamental flow characteristics which decide the nature of vacuum generation during the transient start-up period of vacuum ejectors. Flow transients
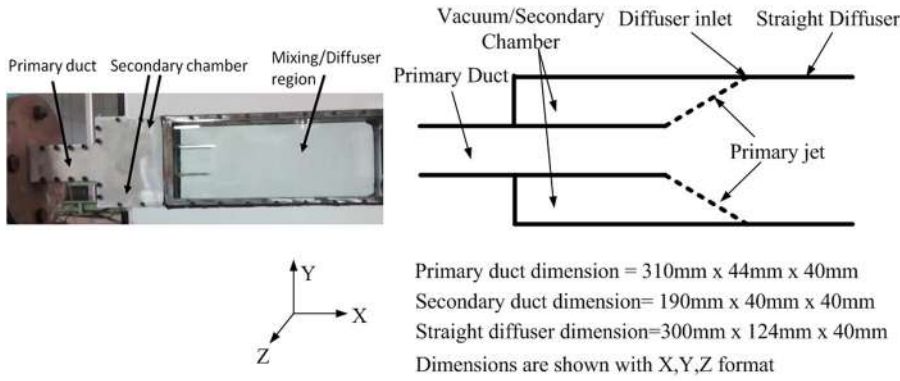
Primary duct dimension = 310mm x 44mm x 40mm
Secondary duct dimension= 190mm x 40mm x 40mm
Straight diffuser dimension=300mm x 124mm x 40mm
Dimensions are shown with X,Y,Z format

(a) Rectangular vacuum ejector test section
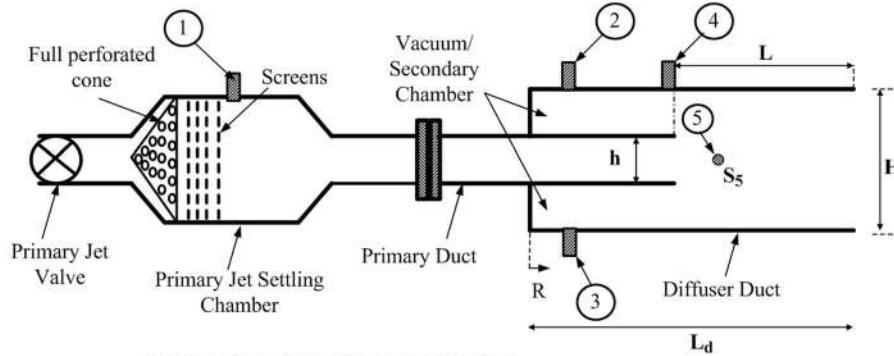
1- Sensor-1 at primary jet settling chamber
2- Sensor-2 at secondary upper section (located at X/H=0.325 from reference R)
3- Sensor-3 at secondary lower section (located at X/H=0.325 from reference R)
4- Sensor-4 at secondary exit section (located at X/H=1.61 from reference R)
5- Sensor-5 at diffuser inlet-S_5 (located at X/H=2.177 from reference R)
L- Distance between primary jet exit plane and diffuser exit plane
L_d- Total length of the outer duct (secondary chamber + diffuser)
H- Diffuser height
h- Primary duct height
H/h=2.82; L/H=2.42; L/L_d= 0.612

(b) Schematic of rectangular vacuum ejector experimental set up and sensor locations

FIG. 2. Rectangular vacuum ejector experimental model.

were studied using time-resolved and time-averaged flow visualization techniques, pressure measurements, and unsteady numerical simulations.

II. EXPERIMENTAL SETUP

In the present study, experiments with both rectangular and round vacuum ejector geometries have been carried out. The details of the experimental models for the rectangular and round cases are shown in Figs. 2 and 3, respectively. For a rectangular model, the jet cannot expand in the Z-direction [shown in Fig. 2(a)] and the aspect ratio of the model is sufficiently large such that the side wall effects will not influence the flow field. Owing to these two reasons, the flow field in the rectangular ejector can be considered to be predominantly two dimensional (2-D). For a round model, the jet can expand in all directions owing to which the flow field will be three dimensional (3-D). The experimental setup consists of the ejector model with a primary duct, a closed secondary duct, and a test section/diffuser, as shown in Fig. 2. The primary duct

(a) Round secondary flow ejector geometry
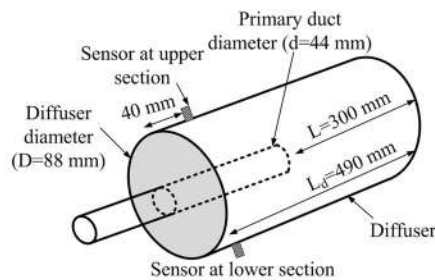
(b) Schematic of round ejector and sensor locations

FIG. 3. Round vacuum ejector experimental model.

is supplied with high-pressure air using the blowdown facility available in the Department of Aerospace Engineering-IIT Madras. The vacuum ejector is started by suddenly opening the blowdown facility and thereby increasing the jet total pressure from the atmospheric condition to higher levels. For the rectangular ejector, the maximum primary pressure achieved during the start-up is 6.8 bars, and for the round ejector it is 7.2 bars. For both the cases, it is ensured that the ejector achieved started mode operation. It should be noted that the primary jet valve opening has been carried out manually and it is hard to repeat the experiments with the same pressure conditions and opening rates. To address these issues, multiple experiments have been conducted with various maximum primary pressure conditions and pressure ramping rates. It is found that the nature of vacuum generation is independent of the ramping rate and the maximum primary jet pressure conditions. Further details regarding this study can be found in Appendix A.

The current experimental study consists of flow visualization of a diffuser and static pressure measurements in the secondary/vacuum chamber. Transient flow visualization was carried out by capturing the density gradients along the flow direction using the time-resolved schlieren imaging technique. A conventional Z-type schlieren system was used in the experiments. Images of the flow fields were captured at 3600 frames per second (fps) and 10 μs exposure time using a PHOTRON FASTCAM SA-4 high-speed camera. The flow visualization technique based on the particle tracer method (Mie-scattering) was also employed to visualize the recirculating flow during start-up. A combination of smoke particles (generated from joss stick) and talc powder has been used to generate the tracer particles since the smoke particles will be a better choice for the initial low-speed flow, and the talc powder will be more suitable for the high-speed flow during the later period of the start-up. In the present study, the conventional way of supplying the seeding particles continuously into the flow system cannot be employed during the start-up since this will alter the vacuum levels being achieved in the chamber. Due to this limitation, the talc powder has been uniformly spread over the top of the primary duct, and the joss stick which was fixed leak tight in the vacuum chamber has been ignited to release the smoke prior to the starting of zero secondary flow

ejector operation. The ejector is then started by suddenly opening the primary jet valve, and the flow evolution in the vacuum chamber and in the diffuser has been recorded simultaneously, using the high-speed camera. The frame rate and the sensor exposure time used in the powder flow visualization study are the same as that of schlieren experiments. It is to be noted that the powder flow visualization in the present study is not able to provide the details of flow evolution for the entire start-up period since there is no continuous supply of seeding particles. However, the initial transients are captured which is expected to give an insight into the development of recirculation bubbles in the diffuser and in the vacuum chamber.

Pressure variations in the vacuum chamber and the blowdown settling chamber were also measured using piezoresistive sensors of KELLER make. The pressure sensors were flush mounted with the walls. The sensitivity of the sensor is 0.9 V/bar with a full-scale reading of 10 bars. Pressure data acquisition was carried out with a sampling frequency of 2 kHz. The pressure data acquisition and the schlieren imaging were synchronized to obtain the time traces of the flow pressure data in accordance with the flow field images. Further details regarding the synchronization technique can be found in the previous paper by the authors.[19]

III. COMPUTATIONAL DETAILS

A. Rectangular ejector

Computational fluid dynamics (CFD) simulations for the rectangular ejector have been carried out by solving two dimensional transient compressible Reynolds averaged Navier-Stokes equations, using a commercial CFD package ANSYS FLUENT 14.0. A schematic of the computational domain is shown in the inset of Fig. 4(a). In the present simulations, a transient pressure inlet boundary condition (from the experimental settling chamber pressure-time history) has been used in the primary duct inlet. An extended domain (5H in the Y-direction and 20H in the X-direction) has been created toward the exit of the primary duct to specify the pressure outlet (ambient) boundary condition. The details of the computational method used for the present simulation are shown in Table I.
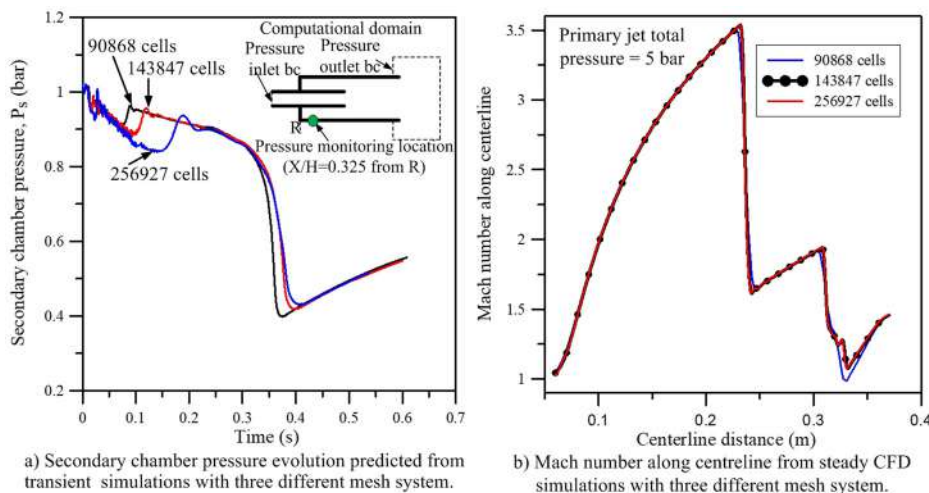
FIG. 4. Mesh independence study for the rectangular ejector case based on unsteady and steady simulations.

a) Secondary chamber pressure evolution predicted from transient simulations with three different mesh system.

b) Mach number along centreline from steady CFD simulations with three different mesh system.

TABLE I. Computational details.

Spatial discretization	Second order
Transient formulation	Second order implicit
Flux discretization	Roe-FDS
Time step	10^{-6} s
Turbulence model	SST k-ω

The computational domain has been discretized using quadrilateral cells. In order to arrive at an optimum mesh, a mesh independence study has been carried out using unsteady simulations. Figure 4(a) shows the evolution of secondary chamber pressure with increase in the primary pressure for three different mesh systems. The time step used for all the cases is 1×10^{-6} s, and the computational details used for the simulation are shown in Table I. It is seen from Fig. 4(a) that any increase in the mesh count above 143 847 cells does not yield a significant change in the secondary vacuum generation process (except during the initial start-up), thus producing a mesh independent solution. The deviation in the secondary vacuum prediction in the initial stage is due to the asymmetric expansion of the jet similar to the well-known asymmetric expansion in suddenly expanding flow in backward facing step geometry.[23–25] The asymmetry in flow might be triggered by the asymmetric turbulent fluctuations at the top and bottom of the primary jet. These turbulent fluctuations are very sensitive to the grid size, and hence the prediction of onset of asymmetric expansion from CFD is also very sensitive to the grid which, in turn, results in deviation in pressure predictions during initial periods with modification in grid spacing. A mesh independence study based on the steady state has also been performed. Figure 4(b) shows results of the mesh independence study for the rectangular ejector (steady state simulation), where the centerline Mach number for three different meshes with the same boundary conditions is plotted. It is seen from Fig. 4(b) that a mesh size of 143 847 cells produces a mesh independent solution.

In order to find whether the current time step (t = 1 × 10^{-6} s) is an optimum time step or not, a time step independence study has been performed by simulating with three time steps: 2×10^{-6} (2t), 1×10^{-6} (t), and 5×10^{-7} (t/2). These simulations are carried out on a mesh system with 143 847 cells. It is seen that decreasing the time step beyond 1×10^{-6} s does not produce much variation in the solution [Fig. 5(a)], and hence this time step has been used for all further simulations.

In order to validate the CFD simulation, the secondary chamber pressure time history from the CFD simulation has been compared to the experimental data and is shown in Fig. 5(b). It can be observed from Fig. 5(b) that the CFD prediction qualitatively agrees well with the experimental data. However, there are some discrepancies in the quantitative predictions, such as the lack of large scale perturbations during un-started mode, under-prediction of mean pressure in the early period of un-started mode, and over-prediction of mean pressure in started mode. The lack of initial fluctuations in CFD might be due to the fact that the CFD simulation uses two-dimensional equations, whereas the actual experimental geometry has a span-wise dimension too. This may induce some 3-D effects which are not modeled in CFD. The over-prediction in the pressure value after the started mode might be due to the in-accuracy of the present turbulence model in predicting the shear layer growth and its impingement with the outer wall. Since the primary flow is bounded by the shear layer, the effective area to which the primary jet expands depends on the shear layer thickness and the error in this prediction might strongly affect the predicted Mach number at the jet attachment point and hence the pressure values as well. In the present work, however, the CFD results are used only to qualitatively assess the flow fields and hence the quantitative mismatches may be ignored without losing the fidelity of the predictions as the qualitative comparison is very good.

B. Round ejector

For the round ejector case, three-dimensional compressible Navier-Stokes equations have been solved instead of axisymmetric equations. This is because there is a possibility that the flow may exhibit bi-stable characteristics as in the case of suddenly expanding symmetric ducts[23–25] and an axisymmetric model will not be able to predict the bi-stable flows. The
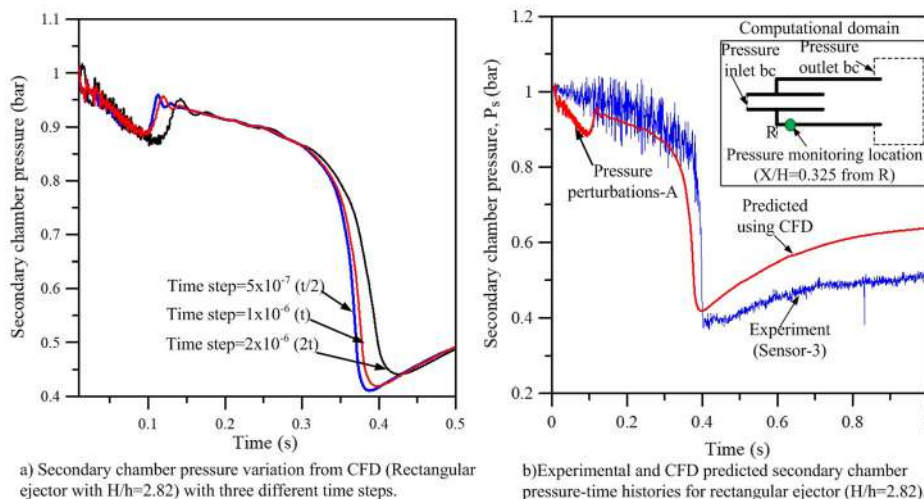

a) Secondary chamber pressure variation from CFD (Rectangular ejector with H/h=2.82) with three different time steps.

b) Experimental and CFD predicted secondary chamber pressure-time histories for rectangular ejector (H/h=2.82).

FIG. 5. Time independence and validation study for rectangular ejector simulation (H/h = 2.82).

a) Mach number along centreline from steady CFD simulations with three different mesh system.

b) Experimental and CFD predicted secondary chamber pressure-time histories for round ejector (D/d=2).

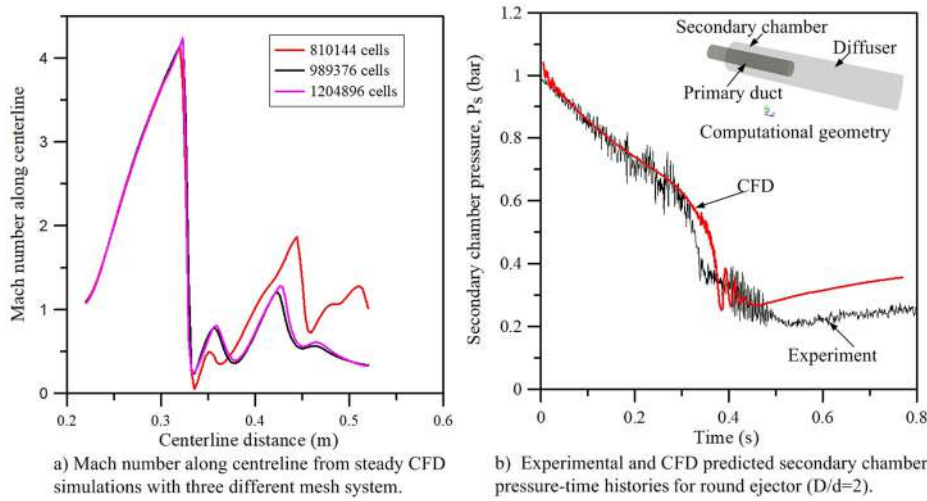FIG. 6. Mesh independence and validation studies for the round ejector model (D/d = 2).

computational schemes used for the round ejector case are the same as those of the rectangular ejector simulation (Table I). A mesh independence study has been carried out for the round ejector case also by comparing the centerline Mach number for three different mesh systems with the same boundary conditions. Since the transient simulation takes enormous amount of computational time, the mesh independence study has been performed using steady state simulations and the results are shown in Fig. 6(a). It is found that with increase in the mesh size above 989 376 cells, the solution remains invariant of the mesh size. Figure 6(b) shows the vacuum chamber pressure histories during the primary ramping process from the CFD and the experimental studies. It can be seen from Fig. 6(b) that the CFD-predicted results match reasonably well with the experimental data except the region where the vacuum chamber pressure increases with the primary pressure. This is perhaps due to the poor modeling of the shear layer attachment to the diffuser wall, as discussed early.
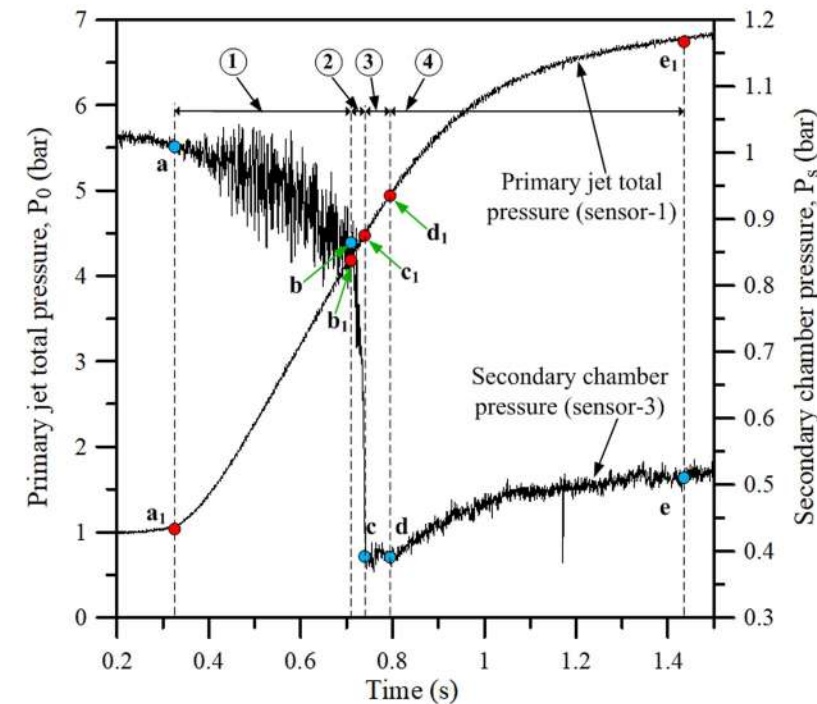

① ⟶ Secondary evacuation with large pressure fluctuations- stage-1(a-b)

② ⟶ Rapid secondary evacuation with very less fluctuations- stage-2 (b-c)

③ ⟶ Stable secondary chamber pressure- stage-3 (c-d)

④ ⟶ Secondary chamber pressure increases- stage-4 (d-e)

Points a_1 to e_1 represents the primary jet total pressures corresponding to the different critical states in the secondary pressure level

FIG. 7. Experimentally measured pressure histories in the primary jet settling chamber and in the secondary chamber.

IV. RESULTS AND DISCUSSION

A. Physics of vacuum generation in the rectangular ejector

This section discusses the fluid dynamics in the rectangular zero secondary flow ejector during its start-up. Figure 7 shows the static pressure evolution in the vacuum chamber while the primary jet total pressure is being ramped up. From Fig. 7, it can be observed that the initial vacuum chamber evacuation progresses in a perturbed and gradual manner (stage-1). The secondary oscillations vanish when the primary jet total pressure reaches a critical value which is then followed by a rapid secondary evacuation process (stage-2). The rapid evacuation terminates when the primary jet total pressure reaches a particular value. Beyond this, there exists a primary jet ramping window over which the vacuum chamber pressure remains more or less the same (stage-3). It is then seen that the secondary chamber vacuum gets destroyed (stage-4) when the primary jet total pressure is ramped above this pressure window.

The overall flow behavior during the different stages of vacuum generation is shown in the schlieren images of Fig. 8. Schlieren images clearly show that the stage-1 evacuation

happens when the ejector operates in the un-started mode. During the un-started mode, the primary jet undergoes an asymmetric expansion, as clearly seen in the schlieren images. The transition from the un-started mode to started mode is characterized by the primary jet expanding to the outer duct with the formation of a Mach reflection (MR) shock structure at the jet attachment point. The attached shear layers seal the vacuum chamber from the perturbations created at the diffuser. Another important thing to notice is that the asymmetric jet expansion transforms to symmetric expansion with the ejector operation switching from the un-started mode to started mode [Figs. 8(c) and 8(d)]. It is seen that with further increase in the pressure, the Mach reflection transforms to a regular reflection (RR) structure, as seen in Figs. 8(d)–8(f). A detailed discussion regarding this can be found in a previous article by the authors.[26] Figure 9 shows the numerical schlieren pictures of the overall flow behavior predicted from the CFD simulations. It is seen that the major flow events, such as the asymmetric expansion, the sealing of the secondary chamber with a Mach reflection shock structure during the started mode, and its transition to regular reflection with increase in the pressure, are qualitatively well captured by the CFD simulation.
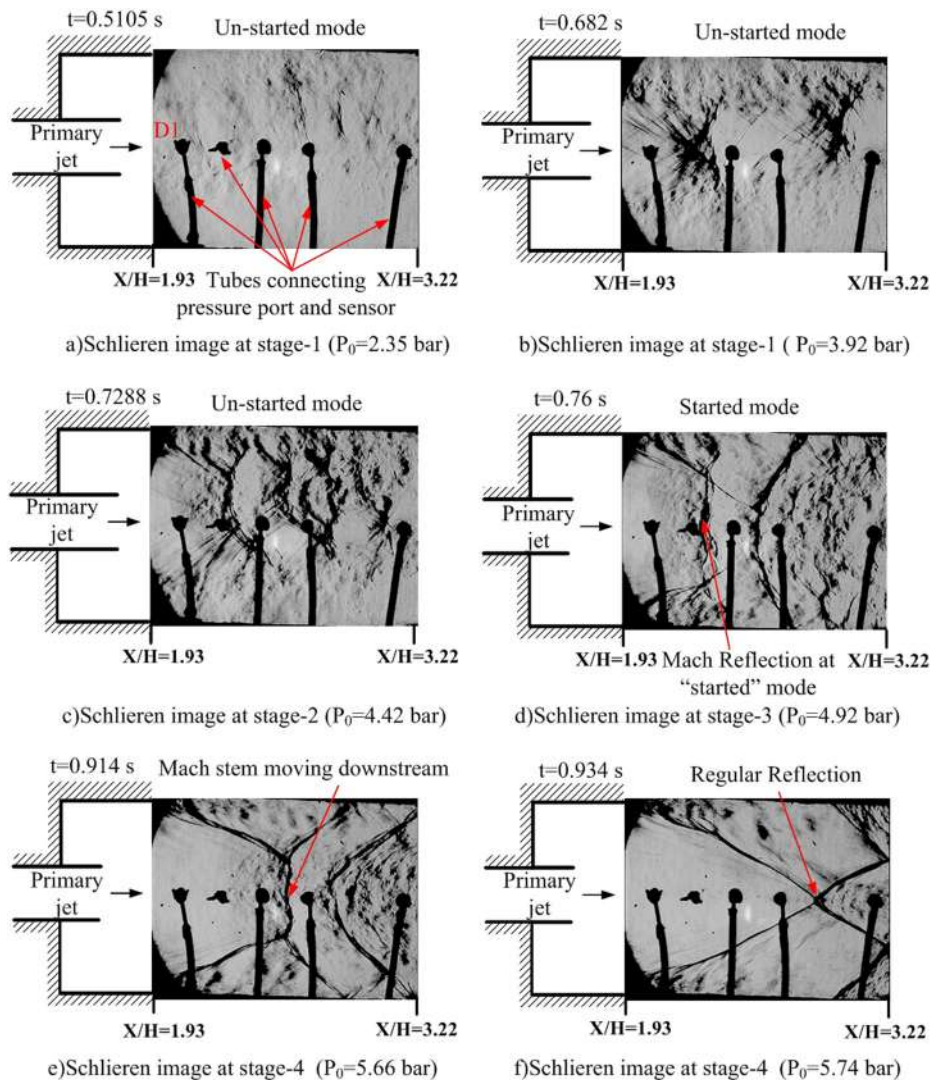

FIG. 8. Time-resolved schlieren images in the diffuser during the primary pressure ramping process.
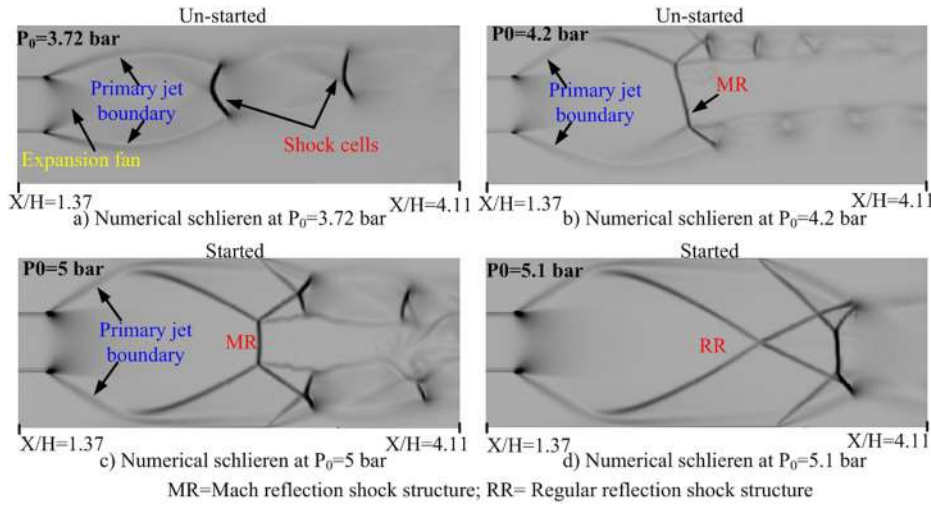
FIG. 9. Numerical schlieren images in the diffuser during the primary pressure ramping process.

The staged evacuation clearly indicates that the fluid induction from the secondary chamber exhibits highly dynamic characteristics with progress in primary pressure ramping. Even though an overall flow behavior during start-up is revealed from the schlieren images, this is not sufficient enough to investigate the reason for the highly dynamic vacuum generation stages. Hence, a thorough understanding of the secondary flow evolution with progress in primary pressure ramping is required and a detailed discussion on this aspect has been given in Secs. IV A 1–IV A 4. In the present study, the fluid flow on the top and bottom of the primary jet during the un-started mode is termed as the secondary flow.
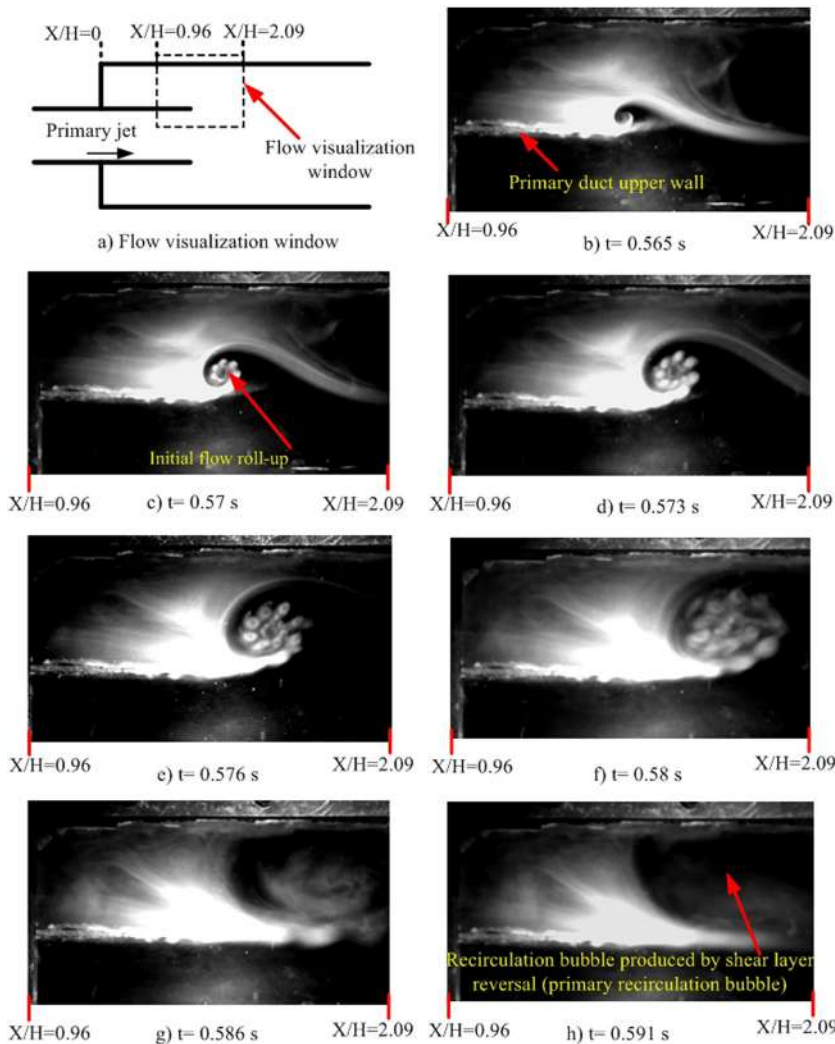

FIG. 10. Flow visualization in the secondary chamber and in the diffuser during the early period of stage-1 evacuation. Here t = 0 refers to the time instant at which camera recording starts (P_0 = 1 bar).

1. Secondary flow characteristics during the stage-1 evacuation process

Stage-1 is characterized with a perturbed and gradual vacuum chamber pressure reduction process (Fig. 7). Past studies based on CFD[19–22] have reported that large recirculation bubbles exist at the top and bottom of the primary jet flow in the diffuser downstream side in the un-started mode. In the present study, the dynamic effects of these recirculation bubbles on the fluid entrainment from the secondary chamber have been investigated using experimental and numerical flow visualization.

Figure 10 shows the powder/smoke flow visualization images during the initial start-up period. It is seen that as soon as the primary flow is established, the shearing action between the primary and secondary flow results in flow roll-up. At this point, it is not clear whether these roll-ups are K-H instabilities developing in the circumferential direction or the shedding of starting vortices combined with the K-H instability. As the primary pressure increases further, the initial flow roll-up grows circumferentially, as seen in Figs. 10(c)–10(g). From Fig. 10(h), it is seen that there is a difference in the intensity of light scattered (contrast) in the secondary chamber and in the diffuser (dark in the diffuser and bright in the secondary chamber upstream). This difference by contrast [Fig. 10(h)] suggests that the seeding particles are not inducted downstream and are constrained in the secondary chamber itself. This indicates the presence of reverse flow from the diffuser downstream to the upstream, and this is termed as the primary recirculation bubble in the present study. It is also seen from Fig. 10(h) that the primary recirculation bubble extends near the secondary chamber exit plane and obstructs the fluid induction from the secondary chamber. This clearly suggests that the momentum of the fluid from the reverse flow is acting as a counter momentum, impeding the mass induction from the secondary chamber.

The experimental observations are complemented with the help of flow visualization from transient CFD simulations. Figure 11 shows the instantaneous streamlines predicted from the transient CFD simulation. The instantaneous streamlines are plotted by assuming quasi-steady flow at various time steps. Figures 11(a) and 11(b) clearly show the initial flow roll-up. With further progress in primary pressure ramping, flow reversals occur from the shear layers in the primary jet top and bottom boundaries leading to recirculation zones (primary recirculation bubbles), as seen in Figs. 11(c) and 11(d). These results are similar to the experimentally observed flow patterns during the initial period of stage-1. The instantaneous streamlines predicted from CFD [Fig. 11(d)] also reveal that during the un-started mode, fluid from ambient air is inducted into the diffuser duct upstream through the gap formed between the reversed shear layer flow and the diffuser wall. This induction is due to the low pressure existing at the diffuser upstream due to the expansion of the primary jet. This inducted flow cannot take a sharp turn and attach to the diffuser wall, and as a result, a small recirculation bubble appears (apart from the primary recirculation bubble) at the exit of the diffuser duct [Fig. 11(d)].
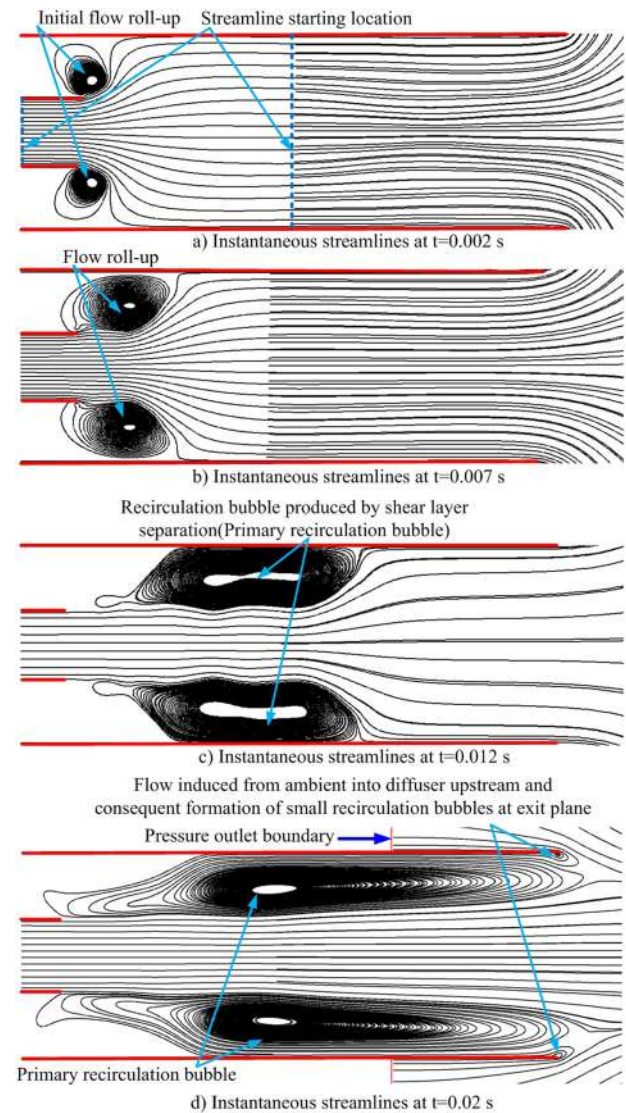

FIG. 11. Instantaneous streamlines (from CFD) with progress in primary pressure ramping during the initial period of the stage-1 evacuation process.

It is expected that the existence of the reverse flow in the diffuser influences the fluid flow in the secondary chamber too. This has been investigated using the powder flow visualization images. Figure 12, which is a continuation of Fig. 10, reveals that the interaction of the primary recirculation bubble with the fluid in the secondary chamber results in the formation of another recirculation bubble (secondary recirculation bubble) in the vacuum chamber along with the primary recirculation bubble. Velocity vectors predicted from the CFD show that the secondary fluid initially exhibits to and fro motion with progress in primary pressure ramping (Fig. 13). This initial to and fro motion settles down at a later time instant to form a secondary recirculation bubble in the vacuum chamber along with the primary recirculation bubble, as shown in Fig. 13(d). Thus the CFD simulation also confirms the presence of experimentally observed recirculation bubbles in the secondary chamber and in the diffuser, during the stage-1 operation. The existence of the secondary recirculation bubble suggests that the fluid entrainment from the secondary chamber will be marginal during the initial start-up. Flow visualization experiments also
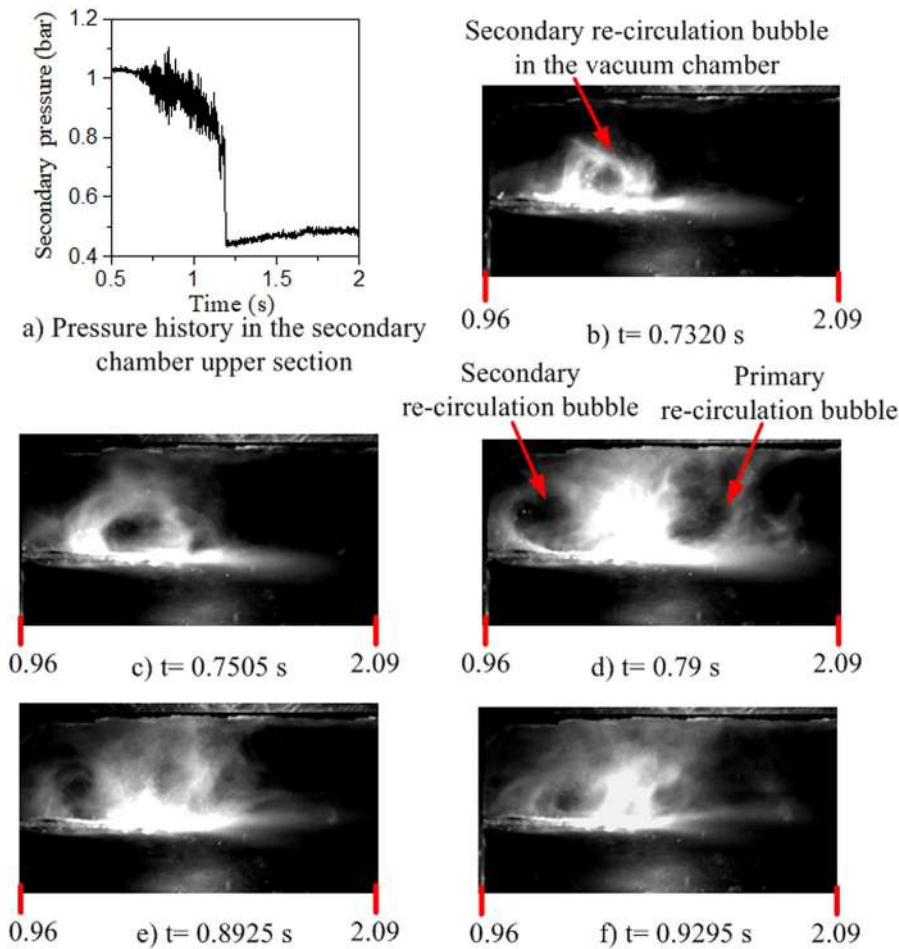
FIG. 12. Flow visualization in the secondary chamber and in the diffuser during the later period of stage-1 evacuation. Here t = 0 refers to the time instant at which camera recording starts.

show that the primary and secondary recirculation bubbles are subjected to oscillations, possibly due to downstream perturbations, which in turn oscillate the secondary flow. The pressure perturbations in stage-1 might be due to these flow oscillations.

From the experimental and CFD observations, it is clearly seen that the existence of the reverse flow from the shear layer and the inducted flow from ambient air into the duct prohibits the entrainment of fluid from the secondary chamber during most of the un-started mode of ejector operation. This can be attributed to the reason why the initial secondary chamber evacuation progresses with a slow rate. However, the slow rate of evacuation suddenly vanishes, which is followed by rapid vacuum generation, when the primary jet expansion reaches a critical level (Fig. 7).

2. Secondary flow characteristics during the stage-2 evacuation process

Figure 7 show that stage-2 is characterized with a rapid vacuum generation process. It is to be noted that the vacuum generation will be closely linked to the fluid induction from the secondary chamber. Figures 14(a) and 14(b) show the CFD predicted mass flux crossing the mid-section of the secondary chamber at the secondary top and bottom, respectively, with increase in primary pressure ramping. It is clearly evident from Fig. 14 that the rapid pressure reduction (stage-2) is associated with a rapid increase in mass induction from the secondary chamber. It is also seen from Fig. 14 that before the

rapid evacuation stage, the mass induction from the secondary chamber is very small and remains more or less constant and this quantitatively confirms the gradual evacuation in stage-1, as qualitatively observed in the powder flow visualization images (Fig. 10).

Figure 15 shows the comparison of computationally predicted static pressure histories in the vacuum chamber (right side of Fig. 15) and the corresponding evolution of flow through instantaneous streamline plots (left side of Fig. 15). It is observed from Figs. 15(a)–15(e) (left side) that with increase in the primary jet total pressure or primary jet expansion level, the high momentum primary jet expands and brings the shear layer closer to the diffuser wall and subsequently reduces the area of the primary recirculation bubble at the maximum primary jet expansion point. This might result in a situation where the majority of the fluid from the reverse flow into the secondary chamber will be entrained by the high momentum primary jet at the maximum jet expansion point itself. As a result of this, a majority of the fluid supply from the reverse flow is now not reaching the secondary chamber, resulting in the sudden reduction of the impedance against the fluid entrainment from the secondary chamber, leading to the onset of rapid vacuum generation.

This has been quantitatively investigated by computing the CFD-predicted mass flux from the reverse flow in the negative-X direction at various time steps and comparing it with secondary chamber pressure evolution, as shown in
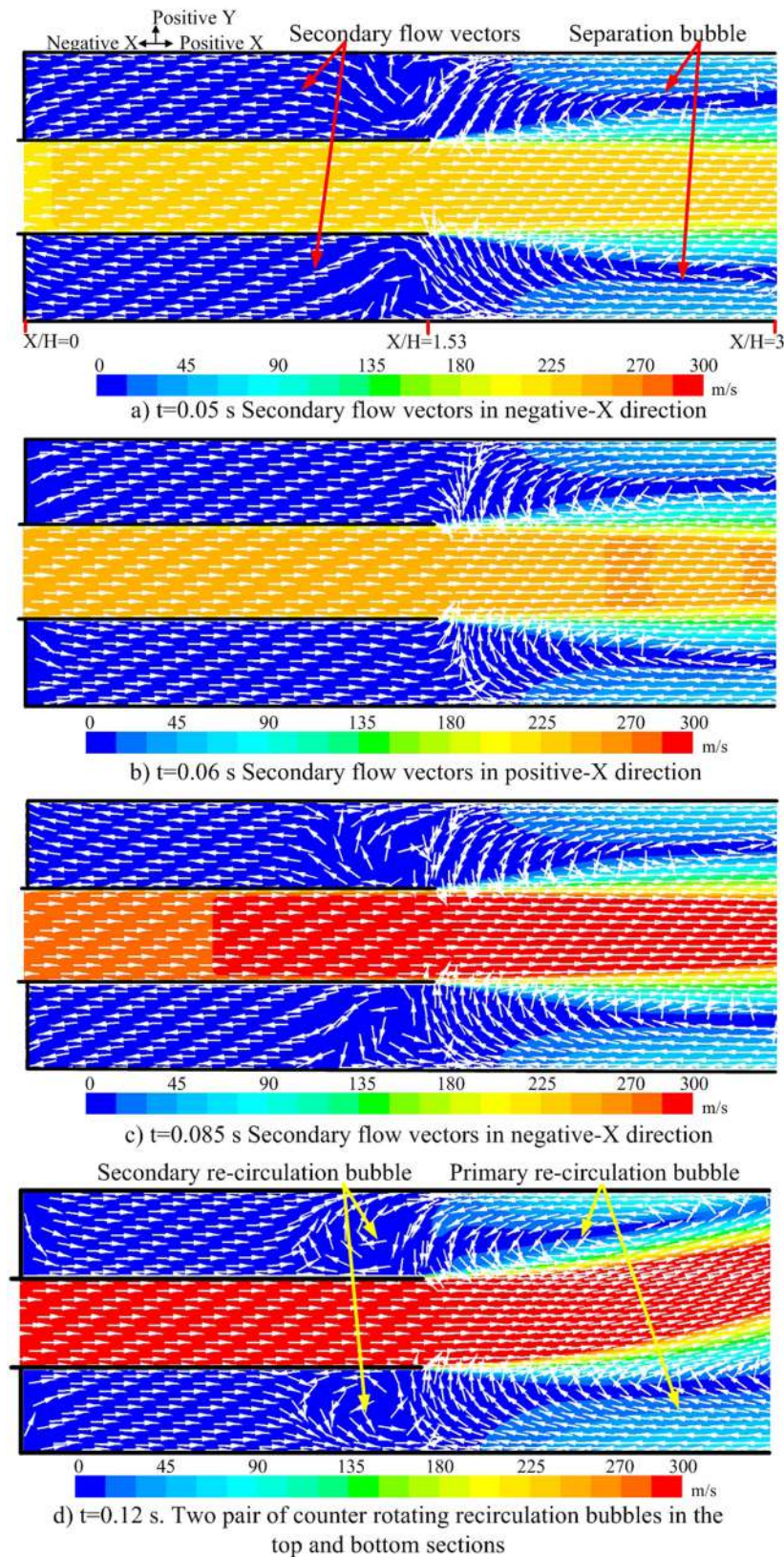
FIG. 13. Evolution of velocity vectors (from CFD) with progress in primary pressure ramping during the stage-1 evacuation process.

Fig. 16. It should be noted that the mass flux from the reverse flow in the negative-X direction is what supplies fluid to the secondary chamber and blocks the mass induction from the secondary chamber exit plane. The mass flux from the reverse flow is calculated at a section where maximum primary jet expansion occurs and a schematic is shown in the insets of

Figs. 16(a) and 16(b). Figure 16(a) shows the pressure and mass flux evolution in the secondary top, and Fig. 16(b) shows the evolution of these quantities in the secondary bottom. A detailed explanation of the procedure for computing the reverse flow mass flux is given in Appendix B. From Figs. 16(a) and 16(b), it is clearly seen that the rapid evacuation stage
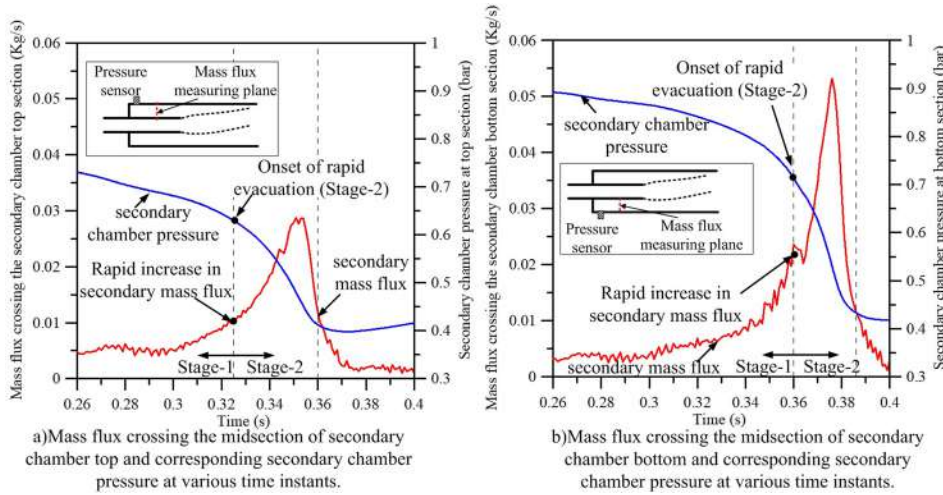
FIG. 14. Mass flux crossing the midsection of the secondary chamber and corresponding secondary chamber pressure at various time instants.

a)Mass flux crossing the midsection of secondary chamber top and corresponding secondary chamber pressure at various time instants.

b)Mass flux crossing the midsection of secondary chamber bottom and corresponding secondary chamber pressure at various time instants.

(stage-2) happens, while the reverse flow mass flux in the negative-X direction reduces steeply. The reduction in reverse flow mass flux, as the primary jet expansion reaches close to wall, is due to the fact that the flow area in the negative-X direction near the wall now becomes very small. This results in the induction of major portion of fluid flowing in the negative-X direction back into the main jet near the maximum primary jet expansion point itself. The formation of separate recirculation bubbles to the upstream and downstream of the maximum jet expansion point (splitting of the secondary recirculation bubble) as seen in Figs. 15(b) and 15(e) indeed suggests that the fluid supply from the reverse flow in the negative-X direction is now split between these two bubbles. This is also evident from the velocity vector plot at the secondary bottom shown in Fig. 17. Figures 15(b) and 15(e) also show that the rapid pressure reduction happens along with the splitting of the recirculation bubble. Hence, it is clearly evident from Figs. 15–17 that the rapid secondary evacuation is due to the sudden reduction in the fluid supply from the reverse flow in the negative-X direction which was otherwise reaching the secondary chamber and act as a counter momentum against mass induction from the secondary chamber.

To further confirm this, a new CFD simulation (with rectangular ejector configuration) in which the species transport equation has been solved along with Navier-Stokes equations has been carried out. For the new simulation, the fluid that is coming from the inlet has been prescribed as fluid-1 and ambient air crossing the outlet boundary (extended domain) has been prescribed as fluid-2, with both species having the same properties. A schematic of the problem setup is shown in Fig. 18(a). The separate tagging of fluid entrained from the outlet boundary enables tracking the mass fraction of induced fluid from ambient air that is reaching the diffuser upstream. Figure 18(b) shows the variation of the mass fraction of fluid-2 at a measuring location far upstream of the diffuser [as marked in Fig. 18(a)] and the secondary chamber pressure history with increase in primary pressure ramping. In Fig. 18, the starting transients near the onset of rapid evacuation (from 0.32 s from the starting of the pressure ramping process) have only been plotted instead of the complete evacuation process to closely examine the rapid evacuation process. It is clearly

seen from Fig. 18(b) that close to the rapid evacuation stage, the mass fraction of fluid-2 in the far upstream of the diffuser reduces rapidly. This clearly indicates that with a critical primary jet expansion level, the fluid induced from ambient air into the duct is not reaching far upstream of the diffuser since the induced mass is entrained back into the main jet at a downstream position (maximum jet expansion point). This is consistent with the recirculation bubble splitting occurring at the onset of the rapid evacuation stage.

It is also seen from Fig. 15 that the rapid pressure reduction stage is also associated with the vanishing of the secondary recirculation bubble. This is obvious since the rapid evacuation results in sudden draining of the fluid from the secondary chamber (as seen in Fig. 14) which in turn destroys the secondary recirculation bubble. The powder flow visualization images (Fig. 19) also show that the secondary recirculation bubble vanishes with the onset of rapid evacuation. With reduction in the vacuum chamber pressure, the primary jet undergoes further expansion, which eventually results in the expansion of the primary jet up to the diffuser wall or the started mode operation of the ejector.

In the previous study by the authors,[19] it was reported that the sudden evacuation is due to the Fabri choking[27] phenomenon in the secondary stream passage due to the area reduction (due to primary jet expansion) and subsequent velocity increase in the secondary stream. However, the present study reveals that it is not the secondary choking but the dynamics of the recirculation bubble in the diffuser (Figs. 15–17) which decides the rapid vacuum chamber evacuation. It is also clear from the present study that the secondary induction is not at all uniform during the primary pressure ramping process as it is progressed through the formation of multiple recirculation bubbles in the diffuser and secondary chamber.

3. Secondary flow characteristics during the stage-3 evacuation process

From the experiments, it is observed that stage-3 is characterized with a more or less stable vacuum level in the vacuum chamber, as seen in Fig. 7. The reason for this phenomenon can be found in the previous paper by the authors.[19] Stage-3 also marks the onset of the started mode operation where the

a)Instantaneous streamlines and static pressure in the secondary at t=0.3s

b)Instantaneous streamlines and static pressure in the secondary at t=0.325s

c)Instantaneous streamlines and static pressure in the secondary at t=0.335s

d)Instantaneous streamlines and static pressure in the secondary at t=0.35s

e)Instantaneous streamlines and static pressure in the secondary at t=0.36s
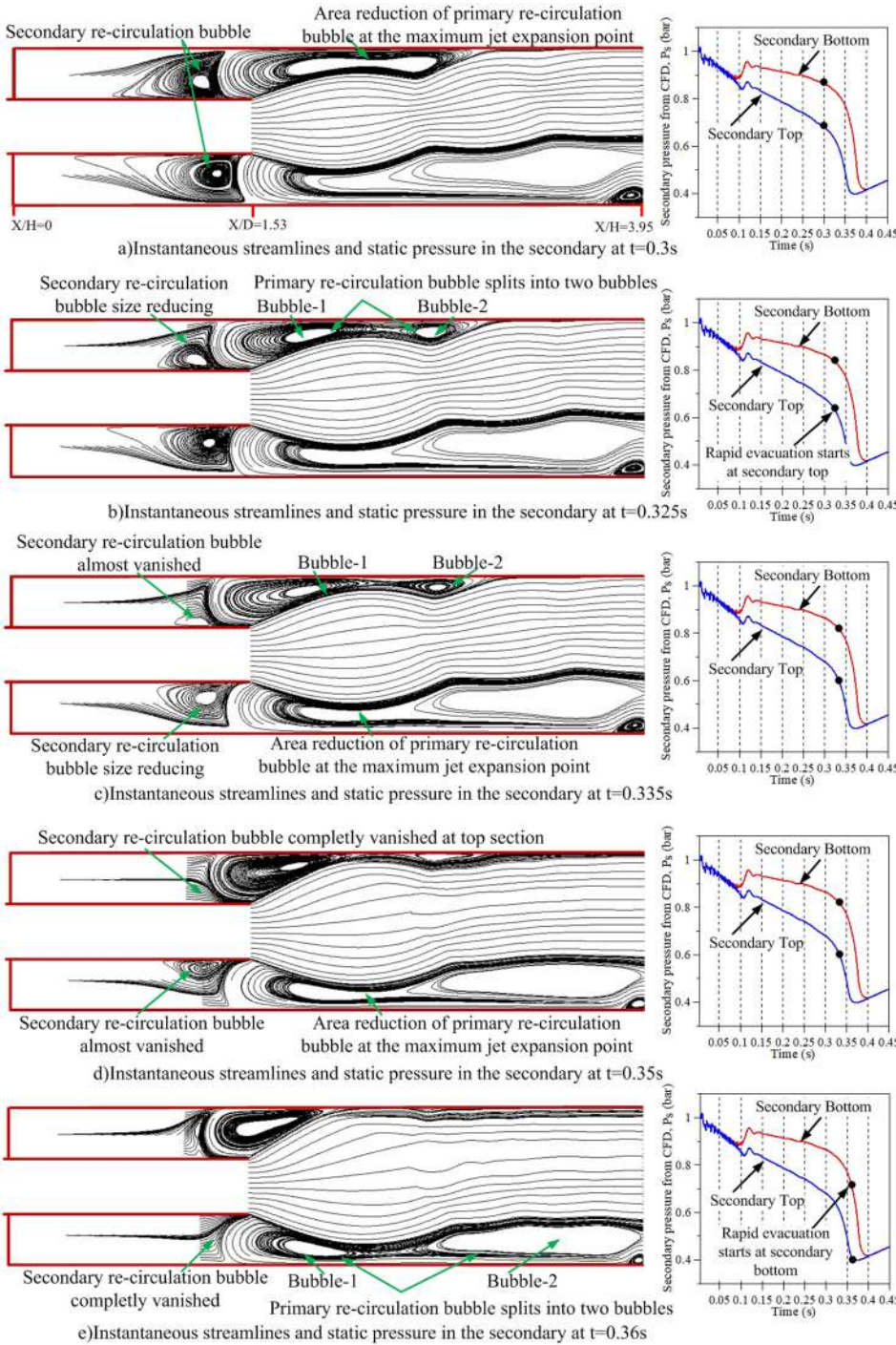
FIG. 15. Instantaneous streamlines (from CFD) with progress in primary pressure ramping during the stage-2 evacuation process.

primary jet expands to the diffuser wall [Fig. 8(d)]. As per the previous understanding,[13,16] the started mode corresponds to the situation where the jet expands to the diffuser wall with the vacuum chamber attaining the minimum possible pressure level, and by this definition, no more jet expansion is possible after the started mode. However, the present study reveals that the primary jet continues to expand after the started mode and eventually ceases at a higher primary jet total pressure compared to the started mode critical pressure. This state is defined as the "frozen" state in the present study. The pressure histories shown in Fig. 20 clearly reveal that the static pressure at the diffuser inlet reduces further (or the primary jet expands further) from the point where the rapid secondary pressure reduction

ceases. The ceasing of sudden vacuum chamber evacuation corresponds to the situation where the primary jet is expanded to the diffuser wall (started mode). The expansion of the primary jet even after attaining started mode might be due to the fact that the shear layer is compressed. This happens as the shear layer has a finite thickness. The secondary chamber vacuum generation ceases when the outer streamline of the shear layer attaches to the diffuser wall. This completely prevents further secondary mass induction and results in started mode operation. The ceasing of primary jet expansion occurs when the inner streamline of the shear layer attaches to the outer duct and after which no more jet expansion is possible. Thus it can be concluded from the experiment that it is not the started
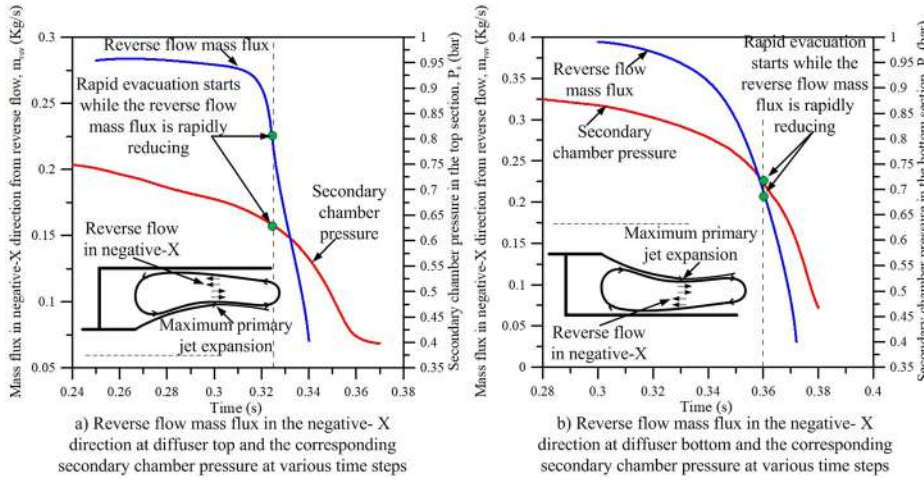
FIG. 16. Reverse flow mass flux in the negative-X direction at the diffuser top and bottom and the corresponding secondary chamber pressure at various time instants.
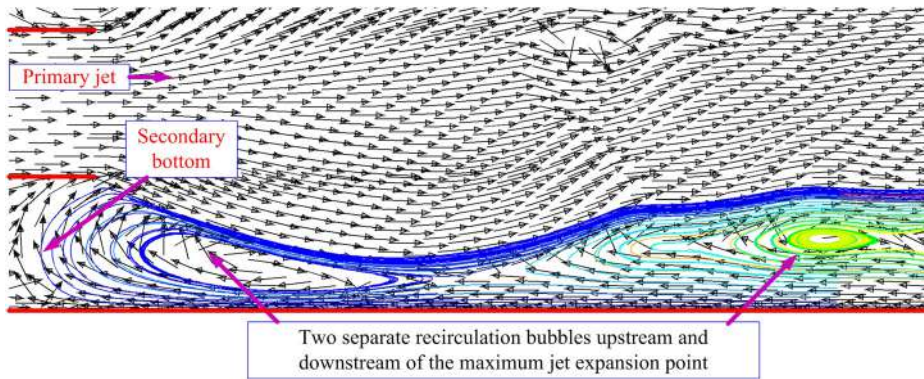
a) Reverse flow mass flux in the negative-X direction at diffuser top and the corresponding secondary chamber pressure at various time steps

b) Reverse flow mass flux in the negative-X direction at diffuser bottom and the corresponding secondary chamber pressure at various time steps

FIG. 17. Velocity vectors at the ejector bottom section showing the formation of two recirculation bubbles at the onset of rapid evacuation.

Two separate recirculation bubbles upstream and downstream of the maximum jet expansion point

mode but the "frozen" state which determines the paradigm shift in the operational characteristics of the vacuum ejector (vacuum generation to vacuum destruction), as seen in Fig. 20.

4. Secondary flow characteristics during stage-4

In stage-4, the static pressure in the secondary chamber increases, destroying the already achieved vacuum levels. As discussed in Sec. IV A 3, the primary jet undergoes further expansion after the started mode but will get eventually restricted by the geometric constriction imposed by the diffuser. After the maximum primary jet expansion stage ("frozen" state), the area ratio at the primary jet attachment point (diffuser inlet area/primary duct area) remains invariant due to the diffuser wall restrictions. As a result of this, the

Mach number at the diffuser inlet will not vary after the "frozen" state," which is clearly observable from the Mach number history at the diffuser inlet shown in Fig. 20. The Mach number history at the diffuser inlet is computed from the static pressure history at the measuring point S_5 (sensor-5) and the jet total pressure history at the settling chamber (sensor-1) using the isentropic relation. The Mach number calculation based on isentropic relations will be valid only after the passage of the initial shock waves in the jet to the downstream of the measuring location. Once the initial shock passes, the underexpanded jet processed by the expansion fan can then be treated as isentropic, assuming that the frictional losses are negligible. Since the Mach number at the diffuser inlet remains constant, an increase in the primary jet total pressure results in an
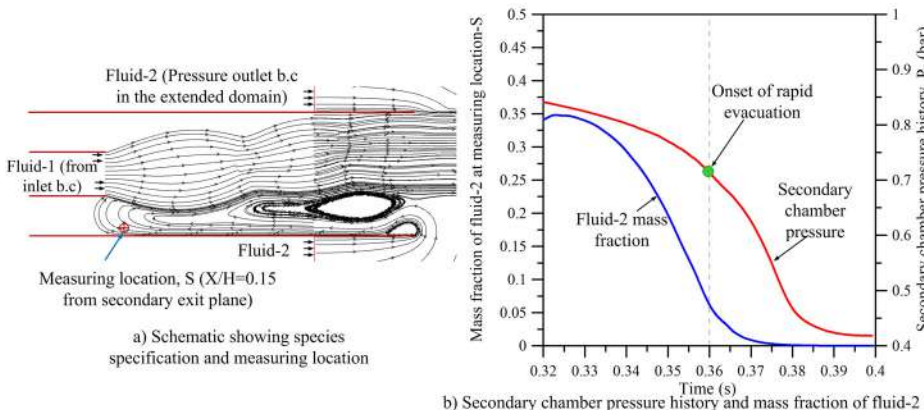

a) Schematic showing species specification and measuring location

b) Secondary chamber pressure history and mass fraction of fluid-2

FIG. 18. Variation of the mass fraction of fluid-2 at the measuring location "S" and the secondary chamber pressure history from CFD with increase in primary pressure ramping.

a) Secondary chamber pressure history

b) t=1.15s. Flow visualization corresponding to point-1 in Figure 19(a).

c) t=1.19s. Flow visualization corresponding to point-2 in Figure 19(a).

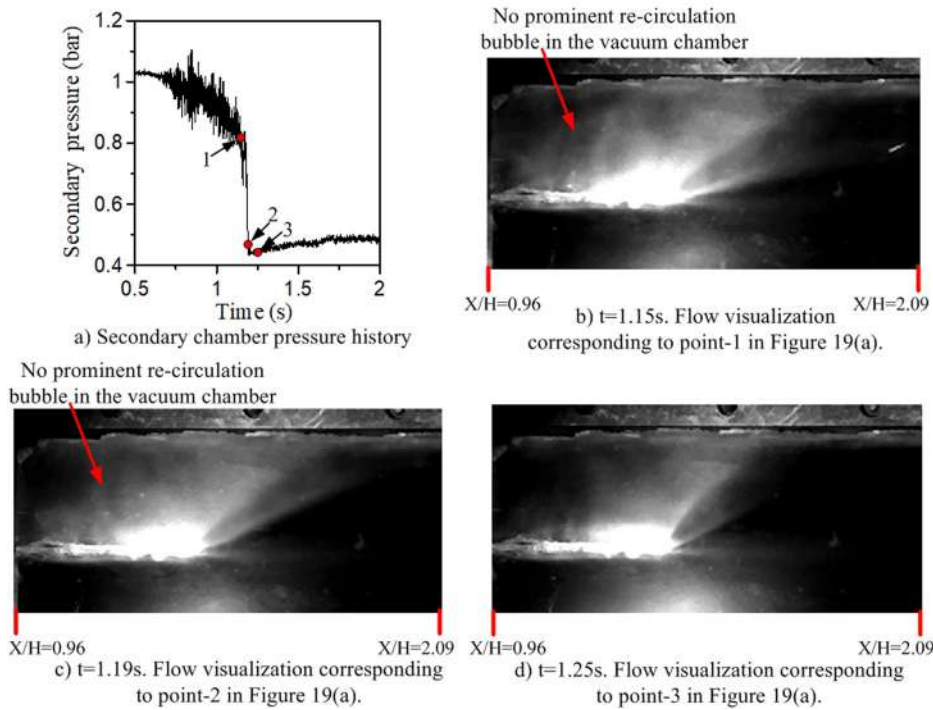d) t=1.25s. Flow visualization corresponding to point-3 in Figure 19(a).

FIG. 19. Flow visualization in the secondary chamber and in the diffuser during the stage-2 evacuation. t = 0 refers to the time instant at which camera recording starts.
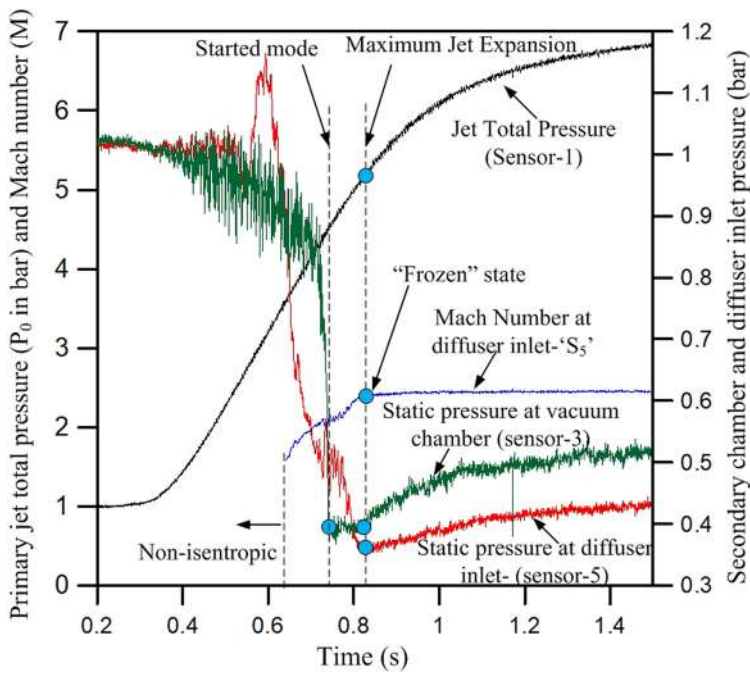

FIG. 20. Experimental pressure histories in the primary jet settling chamber, in the secondary chamber, and in the diffuser inlet and the transient Mach number variation at the diffuser inlet.
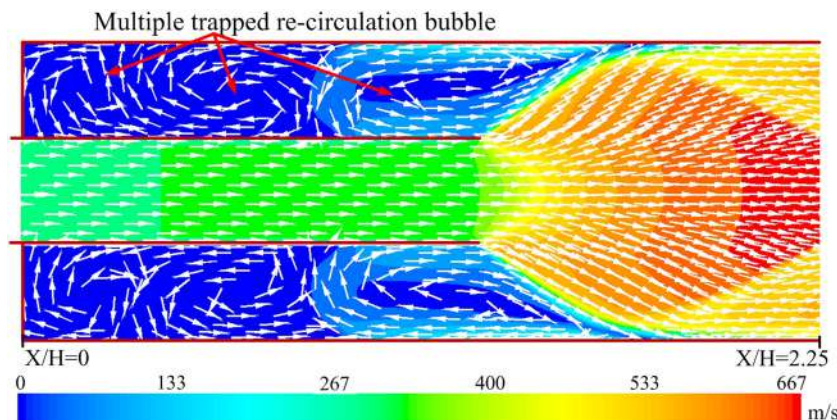

FIG. 21. Velocity vectors (from CFD) with the primary pressure being ramped to 5.8 bars (t = 0.6 s).

a) Secondary chamber pressure history in
round vacuum ejector model with D/d=2

b) Secondary chamber pressure history in
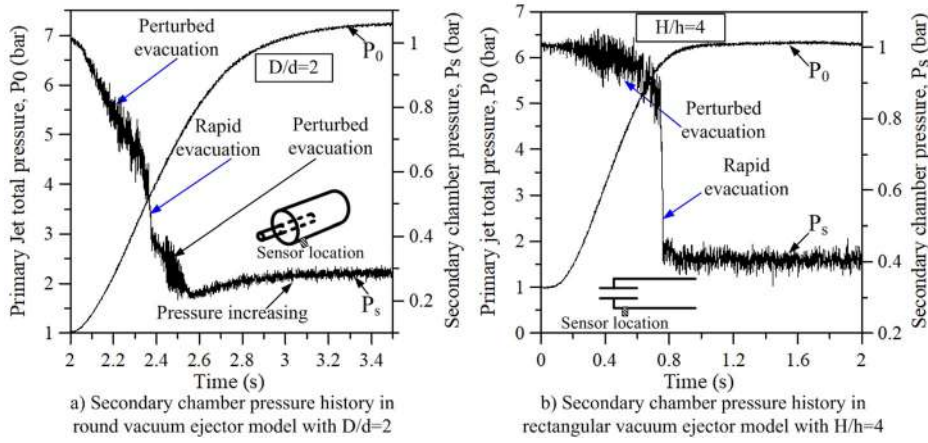rectangular vacuum ejector model with H/h=4

FIG. 22. Experimentally measured pressure histories in the primary jet settling chamber and in the secondary chamber for the round and rectangular ejector configurations.

a)Instantaneous streamlines and static pressure in the secondary at t=0.28s

b)Instantaneous streamlines and static pressure in the secondary at t=0.3s

c)Instantaneous streamlines and static pressure in the secondary at t=0.344s

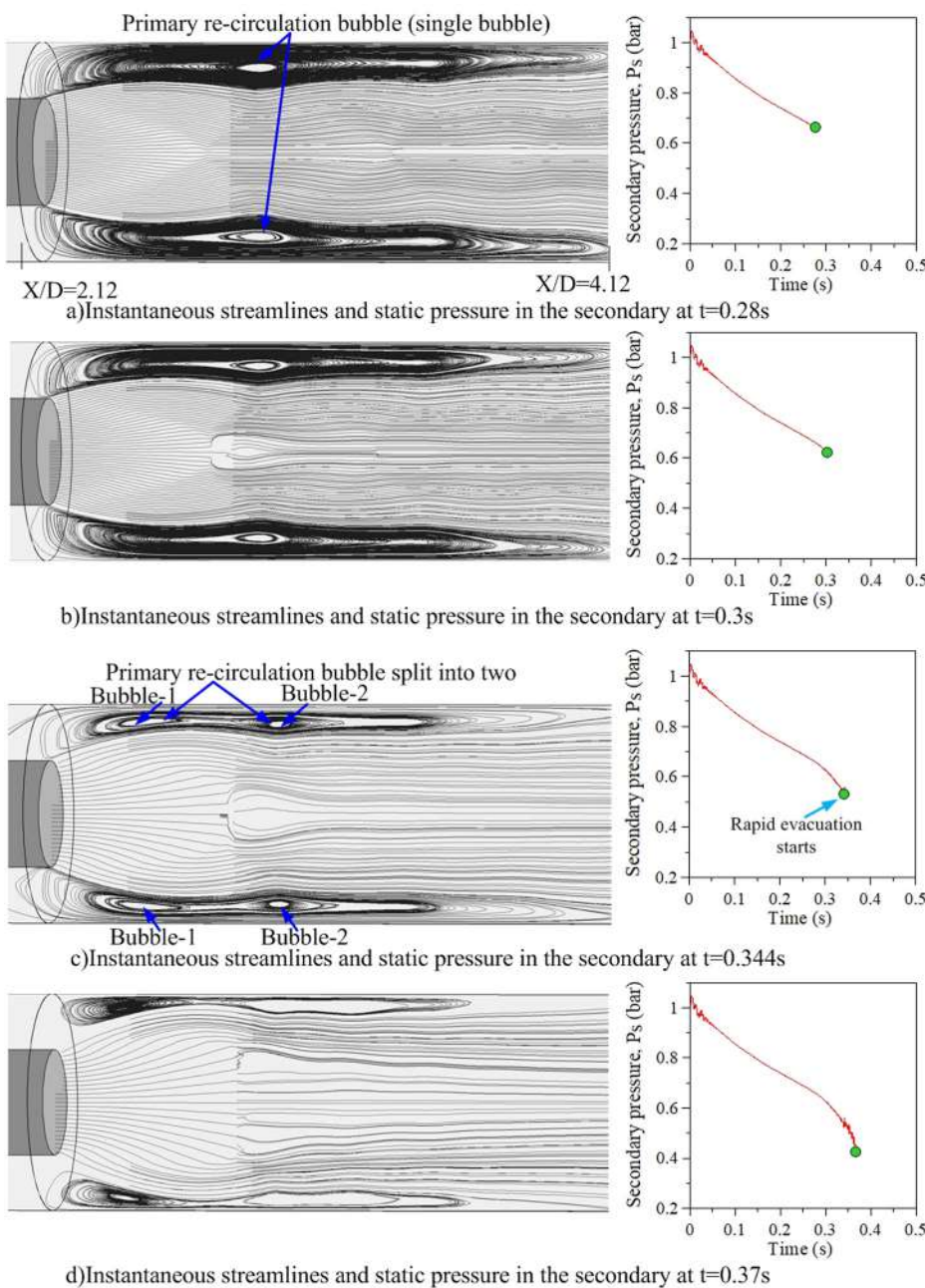d)Instantaneous streamlines and static pressure in the secondary at t=0.37s

FIG. 23. Evolution of CFD-predicted instantaneous streamlines with progress in primary pressure ramping during the stage-2 rapid evacuation process in the round ejector.
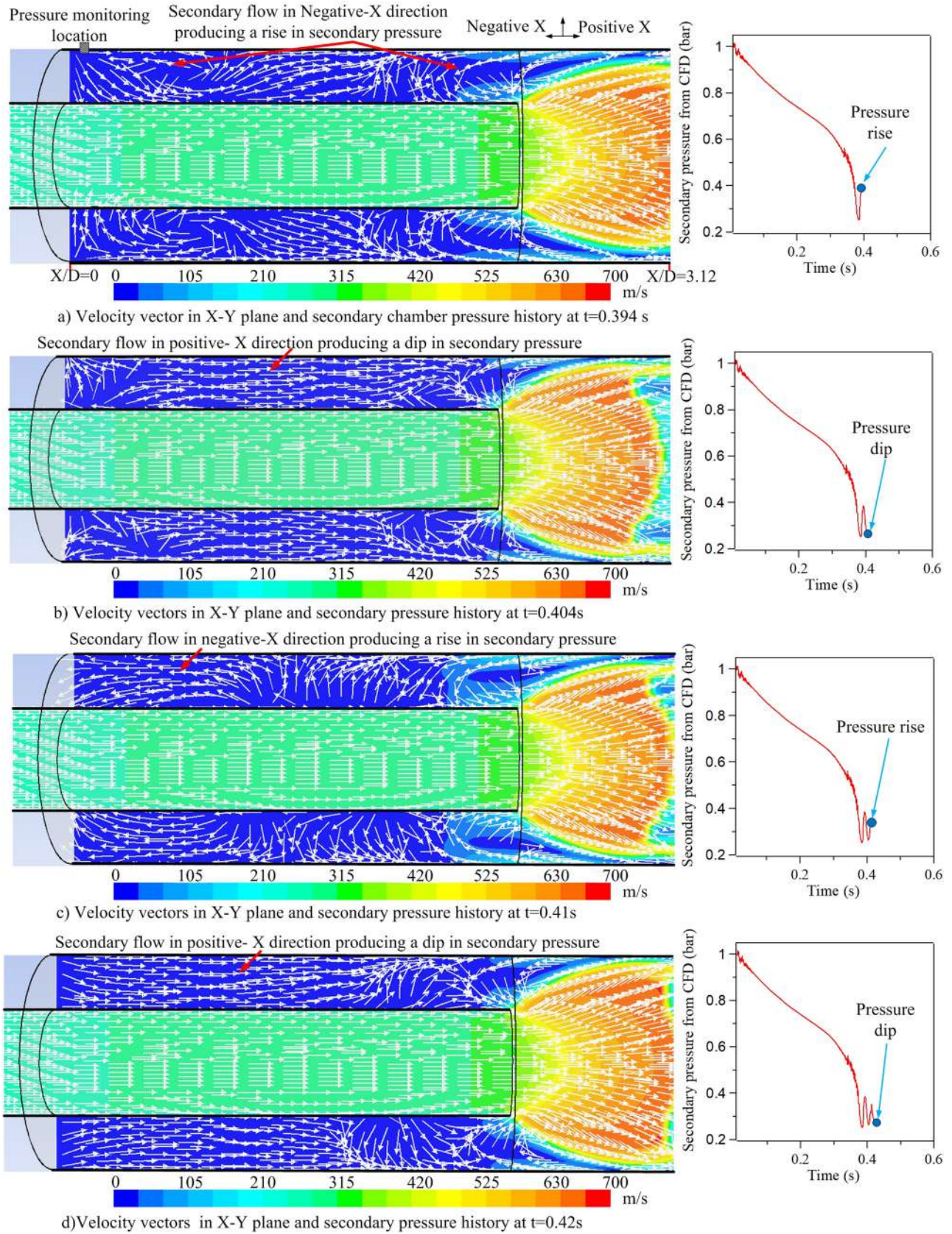
FIG. 24. Evolution of CFD-predicted velocity vectors with progress in the primary pressure after the rapid evacuation process.

increase in the diffuser inlet static pressure (from the isentropic P/P_0 relation) and can be seen in Fig. 20. This might increase the vacuum chamber pressure also, in order to achieve pressure

equilibrium across the shear layer. Another possibility for the vacuum destruction in stage-4 might be due to the impingement of the shear layer with the diffuser wall, which results in

sealing the vacuum chamber from the diffuser. The sealing of the vacuum chamber results in fluid mass addition into the vacuum chamber from the impinged shear layer. The increase in fluid mass results in vacuum chamber pressure build-up. With further increase in the total pressure, the primary jet mass flow rate increases which in turn increases the mass entrainment into the shear layer. This may further increase the fluid mass and the pressure in the vacuum chamber.

At started mode, the impingement of the primary jet with the diffuser wall seals the vacuum chamber from the diffuser section and the diffuser duct will be completely filled with the primary jet alone. The vacuum chamber now has a chunk of more or less stagnant air filled with multiple trapped recirculation bubbles. The velocity vectors overlaid on velocity magnitude contours (from CFD), shown in Fig. 21, clearly reveal this. Due to the large momentum possessed by the primary jet, no recirculation bubbles exist downstream of the diffuser inlet, except those due to the flow separation produced by shock-boundary layer interaction.

B. Physics of vacuum generation in the round ejector

Figure 22(a) shows the experimentally obtained static pressure history in the vacuum chamber with increase in the primary pressure for the round vacuum ejector with D/d = 2. The corresponding rectangular vacuum ejector secondary pressure history (H/h = 4) is shown in Fig. 22(b). It is seen from Fig. 22 that the qualitative nature of vacuum generation for the round case remains more or less same as that of the rectangular case, except that there exists a perturbed vacuum generation stage even after the ceasing of the rapid evacuation stage. This is not seen in the rectangular case. The round ejector vacuum generation physics is further investigated using CFD simulations.

Figure 23 shows the flow evolution through instantaneous streamlines with increase in the primary jet total pressure for the round ejector configuration. It is seen that with increase in the primary pressure, the primary recirculation bubble splits into two as in the case of the rectangular ejector and the rapid pressure reduction occurs in the vacuum chamber. The comparison of instantaneous streamlines (left side of Fig. 23) and the corresponding vacuum chamber pressure (right side of Fig. 23) clearly shows this phenomenon.

Figure 24 shows the evolution of velocity vectors (left side) and the vacuum chamber pressure history (right side) after the rapid evacuation stage. From Fig. 24, it is clearly seen that the vacuum chamber pressure exhibits oscillations even after the rapid evacuation stage. It is clearly seen from the velocity vectors that the secondary flow exhibit to and fro oscillations after the rapid evacuation stage and this might be the reason for the pressure oscillations. These oscillations are also observed in the experimental pressure measurements and are shown as the perturbed evacuation stage in Fig. 22(a). However, the experimental data show large frequency oscillations, whereas the CFD predicted data show low-frequency oscillations. This might be due to the fact that the present simulations are carried out with a second order spatial and temporal accuracy, which makes the numerical scheme in-capable of capturing the higher order frequencies.

V. CONCLUSIONS

Experimental and computational studies on zero secondary flow ejectors revealed that the vacuum generation process during the initial start-up phase is governed by the dynamics of recirculation bubbles in the secondary flow. The presence of recirculation bubbles during the start-up has been experimentally captured through smoke technique for the first time. It is found that during the un-started mode of vacuum ejector operation, large recirculation bubbles exist in the secondary flow in the diffuser region. These recirculation bubbles are produced by the shear layer reversal and the induced flow from ambient air into the diffuser upstream. This reverse flow acts as a counter momentum against the entrainment of fluid from the secondary chamber and results in gradual pressure reduction in the secondary chamber during the initial start-up. The gradual evacuation is followed by a rapid evacuation stage. This is happening at a critical primary jet expansion level where the primary recirculation bubble splits and fluid supply from the reverse flow may not reach the secondary exit plane. This suddenly reduces the impedance acting against the entrainment of fluid mass from the secondary chamber and was identified as the reason for the rapid evacuation. The vacuum is found to be destroyed after the ejector reaches the started mode due to the attainment of the frozen state. The present study also reveals that the nature of vacuum generation in both rectangular and round vacuum ejector geometries is nearly identical.

APPENDIX A: EFFECT OF THE PRIMARY PRESSURE RAMPING RATE ON VACUUM GENERATION

In this section, the effect of ramping time on the nature of secondary evacuation has been investigated. The ramping time is defined as the time required for the settling chamber pressure to rise from the ambient condition to the operating
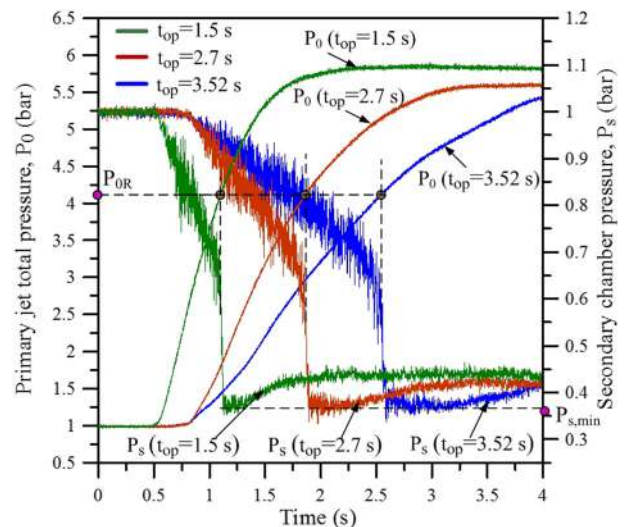
P_{0R} = Primary jet total pressure for attaining rapid evacuation

$P_{s,min}$ = Secondary chamber minimum pressure (started mode)

t_{op} = Primary jet valve opening time (ramping time)

FIG. 25. Secondary chamber pressure histories for cases with a different ramping times.
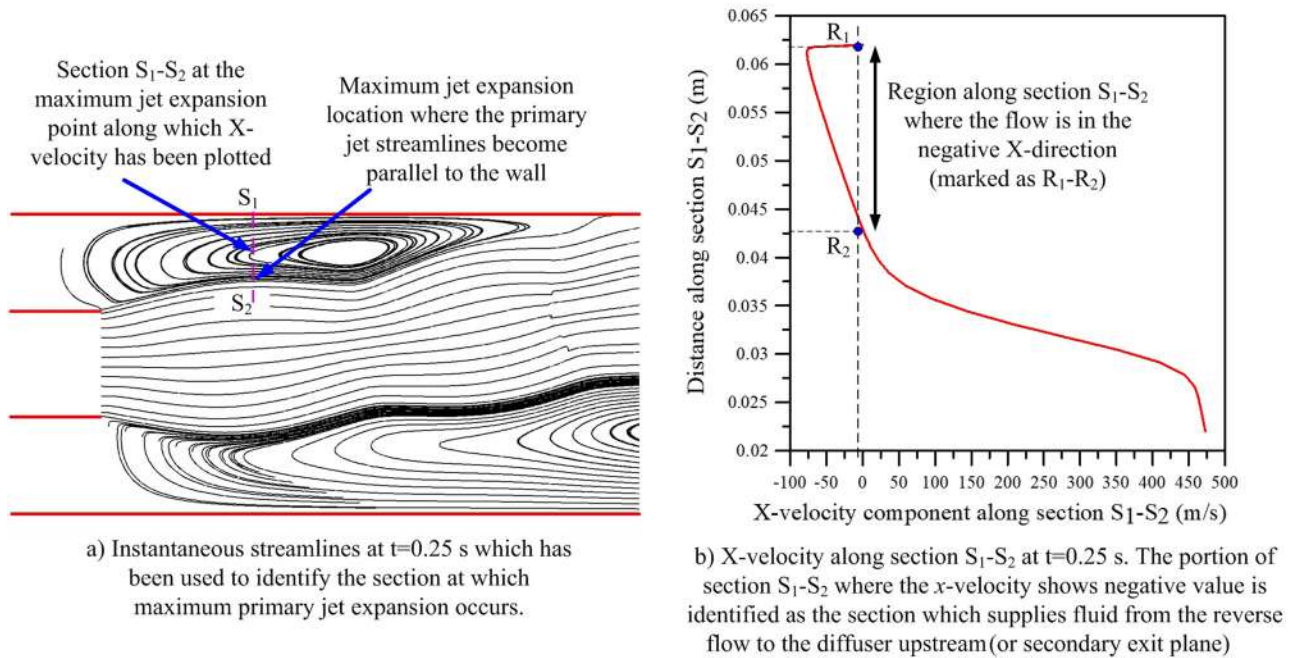
FIG. 26. Instantaneous streamlines and the corresponding X-velocity at the maximum jet expansion section.

pressure. Three cases have been studied with ramping times of 1.5 s, 2.7 s, and 3.52 s. The ejector configuration details used for the study can be found in Fig. 2.

Figure 25 shows the evolution of the jet settling chamber pressure and the secondary chamber pressure with three different ramping times. It is seen that the nature of vacuum generation is the same for all the cases. The primary jet critical pressures for attaining the rapid evacuation (P_{0R}) and the minimum secondary chamber pressure (started mode) are found to be the same for all the cases. From these results, it can be concluded that the primary jet ramping time does not have much influence on the nature of vacuum generation.

APPENDIX B: CALCULATION OF REVERSE FLOW MASS FLUX SUPPLIED TO THE DIFFUSER UPSTREAM

The reverse flow mass flux supplied to the diffuser upstream or the secondary chamber exit plane can be computed by identifying the region along a particular section in the reverse flow where the X-velocity is negative. For this purpose, an X-velocity survey has been carried out at the section where the primary jet expansion reaches the maximum level at various time instants. The maximum primary jet expansion section is identified as the location where the primary jet streamlines become parallel to the wall, as shown in Fig. 26(a). The corresponding X-velocity along the maximum jet expansion section (S_1-S_2) is shown in Fig. 26(b). From Fig. 26(b), the portion of section S_1-S_2 where the X-velocity shows a negative value can be identified as the section which supplies fluid from the reverse flow to the diffuser upstream (or secondary exit plane). This is marked as R_1-R_2 in Fig. 26(b). The total mass flux supplied to the secondary chamber from the reverse flow is calculated by

integrating the mass flux in the negative-X direction crossing the section R_1-R_2.

[1] H. Hu, T. Saga, T. Kobayashi, and N. Taniguchi, "Mixing process in a lobed jet flow," AIAA J. **40**(7), 1339–1345 (2002).

[2] A. V. Sobolev, "Intensification of mixing by small-size jets in ejectors with central nozzle," Thermophys. Aeromechanics **20**(3), 273–276 (2013).

[3] J. Yu, H. Chen, Y. Ren, and Y. Li, "A new ejector refrigeration system with an additional jet pump," Appl. Therm. Eng. **26**, 312–319 (2006).

[4] M. Alperin and J.-J. Wu, "Thrust augmenting ejectors, Part I," AIAA J. **21**(10), 1428–1436 (1983).

[5] M. Alperin and J.-J. Wu, "Thrust augmenting ejectors, Part II," AIAA J. **21**(12), 1698–1706 (1983).

[6] B. J. Huang, C. B. Jiang, and F. L. Hu, "Ejector performance characteristics and design analysis of jet refrigeration system," J. Eng. Gas Turbines Power **107**, 792–802 (1985).

[7] K. Chunnanond and S. Aphornratana, "Ejectors: Applications in refrigeration technology," Renewable Sustainable Energy Rev. **8**, 129–155 (2004).

[8] K. K. Ahuja, "Mixing enhancement and jet noise reduction through tabs plus ejectors," AIAA Paper No. 1993-4347, 1993.

[9] W. L. Jones, H. G. Price, Jr., and C. F. Lorenzo, "Experimental study of zero-flow ejectors using gaseous nitrogen," NASA Technical Note D-230, 1960.

[10] R. C. Bauer and R. C. German, "Some Reynolds number effects on the performance of ejectors without induced flow," Technical Report AEDC-AEDC-TN-61-87, 1961.

[11] B. Mandell, B. L. McFarland, R. E. Nelson, and G. O. Patmor, "Scale model testing of 90 deg supersonic turn ejector systems for altitude simulation," J. Spacecr. Rockets **1**(1), 108–111 (1964).

[12] T. D. Derick, "A general simulation of an air ejector diffuser system," M.S. thesis, University of Tennessee, 2010.

[13] R. C. German and R. C. Bauer, "Effects of diffuser length on the performance of ejectors without induced flow," Technical Report AEDC-AEDC-TN-61-89, 1961.

[14] R. C. Bauer and R. C. German, "The effect of second throat geometry on the performance of ejectors without induced flow," Technical Report AEDC-AEDC-TN-61-133, 1961.

[15] C. J. Wojciechowski and P. G. Anderson, "Parametric analysis of diffuser requirements for high expansion ratio space engine," NASA Technical Note LMSC-11REC TR D784489, 1981.

[16]K. Annamalai, K. Visvanathan, V. Sriramulu, and K. A. Bhaskaran, "Evaluation of the performance of supersonic exhaust diffuser using scaled down models," Exp. Therm. Fluid Sci. **17**, 217–229 (1998).

[17]R. M. Kumaran, P. K. Vivekanand, T. Sundararajan, K. Kumaresan, and D. R. Manohar, "Optimization of second throat ejectors for high-altitude test facility," J. Propul. Power **25**(3), 697–706 (2009).

[18]R. K. Ashok, S. Sankaran, K. Srinivasan, and T. Sundararajan, "Effects of vacuum chamber and reverse flow on supersonic exhaust diffuser starting," J. Propul. Power **31**(2), 750–754 (2015).

[19]R. Arun Kumar and G. Rajesh, "Flow transients in un-started and started modes of vacuum ejector operation," Phys. Fluids **28**, 056105 (2016).

[20]B. H. Park, J. H. Lee, and W. Yoon, "Studies on the starting transient of a straight cylindrical supersonic exhaust diffuser: Effects of diffuser length and pre-evacuation state," Int. J. Heat Fluid Flow **29**(5), 1369–1379 (2008).

[21]A. Mittal, G. Rajesh, V. Lijo, and H. D. Kim, "Starting transients in vacuum ejector-diffuser system," J. Propul. Power **30**(5), 1213–1223 (2014).

[22]V. Lijo, H. D. Kim, G. Rajesh, and T. Setoguchi, "Numerical simulation of transient flows in a vacuum ejector-diffuser system," Proc. Inst. Mech. Eng., Part G **224**(7), 777–786 (2010).

[23]D. Drikakis, "Bifurcation phenomena in incompressible sudden expansion flows," Phys. Fluids **9**(1), 76–87 (1997).

[24]W. Cherdron, F. Durstand, and J. H. Whitelaw, "Asymmetric flows and instabilities in symmetric ducts with sudden expansions," J. Fluid Mech. **84**(1), 13–31 (1978).

[25]F. Durst, J. C. F. Pereirat, and C. Tropea, "The plane symmetric sudden-expansion flow at low Reynolds numbers," J. Fluid Mech. **248**, 567–581 (1993).

[26]R. Arun Kumar and G. Rajesh, "Shock transformation and hysteresis in underexpanded confined jets," J. Fluid Mech. **823**, 538–561 (2017).

[27]J. Fabri and J. Paulon, "Theory and experiment on supersonic air-to-air ejectors," NACA Technical Memorandum 1410, 1958.